Scripta Materialia 188 (2020) 32–36

Contents lists available at ScienceDirect

Scripta Materialia

journal homepage: www.elsevier.com/locate/scriptamat

Microstructural dependence of the incipient to homogeneous flow transition in metallic glass composites

Jonathan M. Gentile[a], Douglas C. Hofmann[b], Jason R. Trelewicz[a,c,*]

[a] Department of Materials Science and Chemical Engineering, Stony Brook University, Stony Brook, NY 11794, United States
[b] Jet Propulsion Laboratory, California Institute of Technology, Pasadena, CA 91125, United States
[c] Institute for Advanced Computational Science, Stony Brook University, Stony Brook, NY 11794, United States

ARTICLE INFO

Article history:
Received 8 May 2020
Revised 23 June 2020
Accepted 24 June 2020

Keywords:
Metallic glass composites
Yield criteria
Shear localization
Flow transition

ABSTRACT

As ductile derivatives of amorphous alloys, metallic glass composites balance high strength with the ability to mitigate catastrophic shear localization, which has long plagued monolithic metallic glasses. In this study, we employ a bonded-interface indentation technique coupled with strain field mapping to identify the governing yield criterion in metallic glass composites as a function of their microstructural length scales. A crossover from the shear plane to maximum shear stress yield criterion is uncovered at a crystalline fraction of approximately 60%, thus signaling an effective transition from incipient to homogeneous flow as the dominant deformation mode of the composite microstructure.

© 2020 Acta Materialia Inc. Published by Elsevier Ltd. All rights reserved.

The realization of ductile bulk metallic glasses (BMGs) has long eluded the materials science community despite our fundamental understanding of their deformation mechanisms and intrinsic limits for accumulating plastic strain prior to failure. [1–3]. Extrinsic approaches involving the introduction of a ductile crystalline phase to produce metallic glass matrix composites (MGMCs) have made the largest strides in expanding the strength-ductility envelope of amorphous alloys [4–7]. A number of studies have provided critical insights into the role of the crystalline phase in promoting enhanced dislocation plasticity [8,9], biased shear band nucleation at amorphous-crystalline interfaces (ACIs) [10–12], and suppressed shear band propagation [13]. Collectively, these mechanisms lead to a transition from incipient to homogeneous flow that depends largely on the composite microstructure [14–17] as well as extrinsic factors such as temperature and strain rate [18].

Behavior intrinsic to the different stages of shear localization in the amorphous matrix, including large-scale diffusional flow via the activation of shear transformation zones (STZs) and its role in shear band nucleation, can contribute to an improved capacity for plastic strain accumulation even in the absence of a ductile crystalline phase. When material volumes are smaller than the effective shear band incubation length scales, homogeneous flow can transpire through distributed STZ activity [19,20]. Alternatively, an increase in the loading rate in a bulk glass promotes the distributed nucleation of many shear bands in lieu of a dominant shear front, which manifests as a more homogeneous plastic response [21–26]. An analogous mechanism was shown to govern plasticity in MGMCs particularly when the indentation plastic zone is confined solely to the amorphous matrix [27]. However, when the plastic zone expands into both phases of the composite, a reduction in the shear band nucleation stress was observed, indicating that ACIs suppress the activation barrier to nucleate a shear band. Dislocation plasticity also has a strong influence on the composite mechanical response, which was demonstrated by a varying degree of twinning and dislocation pile-up impacting the accumulated plastic strain to failure under tensile loading [28]. Overall, the extent that a ductile crystalline phase will accommodate strain during the deformation of MGMCs will largely govern their ability to exhibit a homogeneous plastic response [29]; yet, the microstructural dependence of this transition remains an active area of research in the absence of a definitive approach for quantifying the crossover in the dominant mode of plastic deformation.

In modeling the yield behavior of BMGs, maximum shear stress models have been shown to overestimate their yield stress as they fail to capture the cooperative nature of shear band formation in the process of localization [30]. Several studies investigating shear banding confined within a plastic zone from surface indentation have shown that shear band trajectories are consistent with the expanding cavity model [31–38]. On this basis, a shear plane yield criterion was proposed that necessitates the local stresses along an entire path define the preferred shear trajectory, which led to vastly improved predictions of the stresses for shear band nucle-

* Corresponding author at: Department of Materials Science and Chemical Engineering, Stony Brook University, Stony Brook, NY 11794, United States.
E-mail address: jason.trelewicz@stonybrook.edu (J.R. Trelewicz).

https://doi.org/10.1016/j.scriptamat.2020.06.066
1359-6462/© 2020 Acta Materialia Inc. Published by Elsevier Ltd. All rights reserved.

ation in BMGs [39]. With MGMCs combining two monolithic materials conforming to different yield criteria, the transition from incipient to homogeneous flow should manifest in the nature of the plastic zone and its interaction with the composite microstructure.

In this letter, we employ a bonded-interface indentation technique to quantify the strain distribution within the plastic zone of Zr-based MGMCs containing a dendritic crystalline phase. Through comparison of the experimental strain fields with yield criteria describing the deformation behavior of monolithic amorphous and crystalline metals, we demonstrate an explicit crossover from the shear plane to maximum shear stress yield criterion with increasing crystalline phase fraction. The shift in the dominant deformation mode is therefore understood in the context of the microstructural dependence of the strain accommodation process.

Bulk MGMCs were synthesized through arc-melting pure elements in an Argon atmosphere, followed by suction casting to produce equilibrium BCC crystalline dendrites within the amorphous matrix. To collectively modulate the respective phase fractions and microstructural length scales, the Be content was varied from 12.5 – 19.1 at.% while maintaining mutual ratios of the constituent elements; exact alloy and phase compositions can be found in Gentile et al. [27]. Three MGMC samples with systematically varied Be concentrations and a baseline monolithic BMG of nominally equivalent composition were produced for this study. Quantitative microstructural analysis was performed in a JEOL 7600F scanning electron microscope (SEM) using a minimum of 10 micrographs per sample with thousands of individual dendrite areas and perimeters tabulated from a prescribed image area. SEM imaging of fiduciary arrays used a 2-column array overlap and high-magnification images to map radial shear bands.

To prepare the materials for strain field mapping, samples were sectioned and mounted with each cross-sectional face held in contact to align the orthogonal surfaces for polishing to 600 grit SiC. The two faces of the cross sections were then simultaneously polished to a mirror-like finish while ensuring orthogonality was maintained with the top surfaces. Local displacement fields were tracked using arrays of small Vickers microindents introduced via a Mitutoyo microindenter with a 0.01 kgF load. With the Vickers diagonals not exceeding 10 μm, the center-to-center spacing between adjacent fiduciaries was 25 μm. The two cross-sectional faces were then bonded together using a thin layer of cyanoacrylate adhesive and cured for 24 h. Surface indents centered on the bonded interface employed a 1/16″ diameter tungsten carbide spherical probe loaded to 30 kgF for a total of 15 s. Following indentation, the samples were unclamped and submerged in acetone to dissolve the cyanoacrylate adhesive from the interface.

Flow transitions will inevitably depend on the distribution of plastic strain within the composites, and in turn their microstructural characteristics. Phase fractions and corresponding length scales are shown in Fig. 1 with data summarized in Table 1. The backscatter SEM image in Fig. 1a displays fine dendrites dispersed in the amorphous matrix, and a reduction in the Be concentration produced larger dendrites and interdendritic spacings in Fig. 1b. Following methods for quantifying dendritic microstructures [15,40–42], we calculated the interfacial density to estimate the interdendritic spacing, denoted L_A, as an effective length scale for the amorphous matrix [27] and the dendrite radius, R_D, both of which are plotted against the Be concentration in Fig. 1c. The crystalline phase fraction, V_f^c, decreased with increasing Be, which was accompanied by an increase in the amorphous fraction, V_f^A, as expected in the composite. However, in contrast to the crystalline phase where R_D increased with V_f^c, the increase in V_f^A was accompanied by a reduction in L_A. Collectively, these results indicate that Be slowed the transformation rate during solidification, thus producing composites with a greater amount of retained amorphous

Table 1
Sample designations for the MGM composites and related microstructural characteristics quantified for the crystalline dendrites and amorphous matrix.

Be Content (at%)	Crystalline Phase		Amorphous Phase		Sample Designation
	Volume Fraction, V_f^c	Dendrite Radius, R_D (μm)	Volume Fraction, V_f^A	Interfacial Density, L_A^{-1} (μm^{-1})	Characteristic Length Scale, L_A (μm)	
34.0	0.00	N/A	1.00	N/A	N/A	BMG
19.1	0.48	0.77	0.52	1.36	0.75	MGM-48V_f^c
15.3	0.55	0.99	0.45	1.18	0.87	MGM-55V_f^c
12.5	0.62	1.57	0.38	0.82	1.23	MGM-62V_f^c

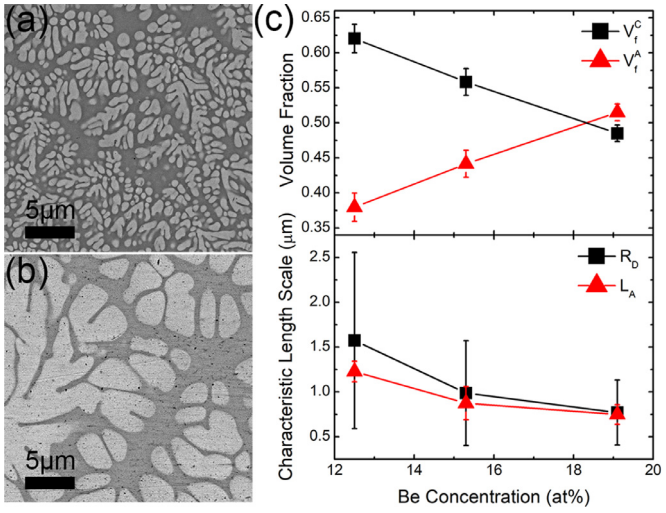

Fig. 1. Representative backscatter SEM micrographs illustrating the dendritic morphology of composites (a) MGM-48V_f^C and (b) MGM-62V_f^C. (c) Volume fractions and characteristic length scales for the amorphous and crystalline phases as a function of Be concentration.

phase and finer microstructural length scales. Recognizing from Fig. 1c that the length scales ranging from 0.5 - 2.5 μm will be invariant relative to the larger plastic zone sizes, our measurements will sample composite network effects and deformation should follow the behavior described by Narayan et al. [43].

To map the strain field beneath the surface indents, we tracked the position of the fiduciary arrays using SEM micrographs acquired on the cross-sectional faces following Ref. [44]. The location of each fiduciary indent on the pre- and post-deformed cross sections was determined as the average of its four corners relative to the axis origin, from which displacement fields were tabulated. Employing a strain-gage rosette analogy, we quantified the in-plane principle strains through knowledge of three measured strains at arbitrary angles as an effective unit cell describing the state of strain at a given position. While this approach ignores the contribution of out-of-plane flow and effectively assumes approximate plane strain conditions, it is a reasonable assumption given the size of the indenter relative to the width of the bonded interface and constraints imposed by the undeformed material [45]. For two-dimensional strain, the principle strains may be evaluated as:

$$\varepsilon_\theta = \varepsilon_{xx}cos^2\theta + \varepsilon_{yy}sin^2\theta + \varepsilon_{xy}sin\theta cos\theta \quad (1)$$

where ε_θ is the strain measured at angle, θ, and ε_{xx}, ε_{yy}, and ε_{xy} are the principle normal and shear strain components. With the two-dimensional strain tensor characterized as a function of position, we calculate each unit cell's local shear strain invariant based on the Von Mises criterion, ε^i_{VM}, as:

$$\varepsilon^i_{VM} = \sqrt{\varepsilon_{xy}^2 + \frac{\varepsilon_{yy}{}^2 + \varepsilon_{xx}{}^2 + (\varepsilon_{xx} - \varepsilon_{yy})^2}{6}} \quad (2)$$

This relationship enables an unbiased, self-consistent quantification of local strain fields after deformation under an arbitrary stress state and has been applied to discretize strain fields in atomistic simulations of BMGs [46]; here, the local shear invariant is determined for each unit cell, which is then plotted in the coordinates of the midpoint of each cell to produce cross-sectional strain maps.

A secondary electron micrograph of an indented cross section for the BMG in Fig. 2a exhibits semi-spherical shear bands in the plastic zone with radial shear bands less prominent as indicated by the arrows, which is a consequence of the boundary conditions in the presence of the bonded free surfaces during spherical indentation. [32,36–38] Bonded-interface indentation using a cylindrical indenter produced only radial shear banding as the elongated cylindrical indenter provides a closer approximation to plane strain. [45] The formation of semi-spherical shear bands in our experiments is thus attributed to deviations from plane strain due to the spherical indentation geometry. Because radial shear bands account for the primary localization mechanism in an expanding plastic zone [31,35], we compared the radial shear bands with shear trajectories calculated using BMG properties reported in Ref. [27]. Plotted as dotted lines in Fig. 2a, the predicted shear band paths are consistent with the shape and magnitude of the radial shear bands as demonstrated in the magnified inset for a selected shear band.

In understanding the process of shear localization, we may compute the corresponding stress along each potential shear trajectory from which the shear plane stress, τ_{sp}, can be determined as the minimum stress along each path [39]. The left half of Fig. 2b illustrates the normalized shear plane stresses for the BMG superimposed over a backscatter SEM micrograph of the indented cross section. The preferred shear path, i.e., the path with the highest sustained stress along its entire length, exhibited a stress approaching 0.07•P_m, where P_m is the mean contact pressure. This path extended from the edge of contact defined as the contact radius, a, to a depth of approximately 2.5a, consistent with shear band morphologies from plane strain indentation experiments. [45] The experimental strain field for the BMG is shown

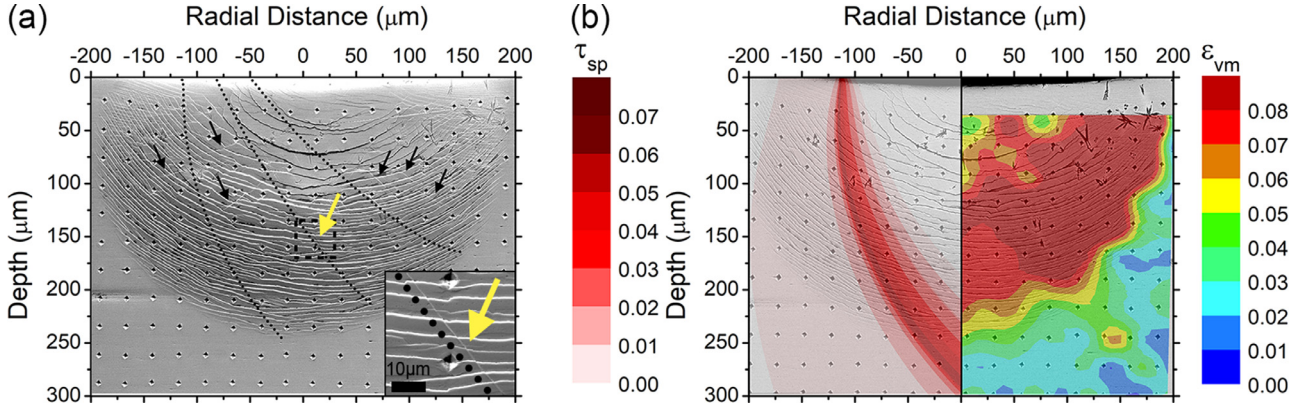

Fig. 2. (a) Secondary electron micrograph of the indented cross section for the BMG showing conspicuous semi-spherical shear banding. Radial shear bands are also present, but are more subtle and thus indexed by arrows with a magnified view in the inset; calculated shear trajectories are indicated by dotted lines. (b) Shear plane stresses plotted in the left half-plane superimposed over a backscatter electron micrograph with the experimental strain distribution in the right half-plane.

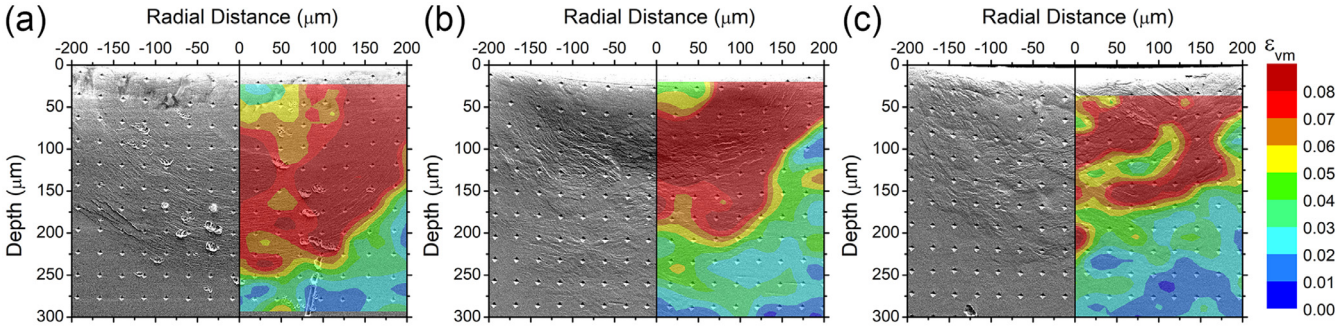

Fig. 3. Secondary electron micrographs of the indented cross sections for samples (a) MGM-48V_f^C, (b) MGM-55V_f^C, and (c) MGM-62V_f^C. The corresponding shear strain distribution is plotted in the right half-plane, which exhibited a collective shift toward the central indenter axis and indentation surface with increasing crystallinity.

on the right of Fig. 2b. The region of high strain generally coincided with the shear band path predicted by the shear plane criterion, indicating that plasticity was accommodated through shear localization and consistent with the formation of radial and semi-spherical shear bands. We note the more distributed nature of the high strain region relative to the predicted shear band path and attribute it to accentuated out-of-plane flow due to the indentation geometry. Further validating the shear plane criterion in describing yield of the BMG is the presence of a low strain region adjacent to the axis of symmetry immediately below the indenter probe, which would not be expected for plasticity governed by the maximum shear stress or pressure-modified yield criteria [39].

With the technique successfully benchmarked on the BMG, we turn our attention to the governing yield criterion as a function of the composite microstructure. Secondary electron micrographs following surface indentation are shown in Fig. 3(a-c) in order of ascending crystallinity with the corresponding shear invariant maps superimposed on the right half of each panel. In the MGM-48V_f^C sample, the formation of semi-spherical shear bands is qualitatively observed to align with the high strain regions in the plastic zone. The bimodal nature of the strain field, which was not present in the BMG, could be due to the partitioning of strain to the dendrites. Nonetheless, the presence of shear bands and overall alignment of the strain field for the MGM-48V_f^C and BMG samples (along both the radial and depth directions) indicates that deformation in this composite is still dominated by shear localization despite the presence of fine crystalline dendrites. With increasing crystallinity, semi-spherical shear bands became less apparent and accompanied by the high strain region converging toward the indentation surface along the primary loading axis. In the MGM-55 V_f^C composite, the high strain region clearly aligned with the plastic zone in Fig. 3b, which exhibited more tortuous shear bands relative to the MGM-48V_f^C sample and indicative of dendrites influencing shear band propagation [47]. Shear banding was completely absent on the cross section of the MGM-62 V_f^C composite in Fig. 3c with the high strain region even more localized near the indentation surface and divided into two distinct regions, clearly demonstrating a shift in the dominant carrier of plasticity relative to the other composites.

For the two extreme cases in Fig. 3, the strain fields are compared with the different yield criteria assuming: (i) shear banding is the dominant carrier of plasticity in MGM-48V_f^C, and (ii) deformation in the crystalline dendrites prescribes to the maximum shear stress yield criterion. The shear plane and maximum shear stress criteria are mapped on the left half of the backscatter electron micrographs for MGM-48V_f^C and MGM-62V_f^C in Fig. 4(a,b), respectively, with the corresponding strain fields on the right. Alignment between the shear plane stress trajectory and the high strain regions in Fig. 4a indicates that plasticity is governed by the shear plane criterion despite the presence of fine crystalline dendrites accounting for 48% of the material; however, the bimodal nature of the strain field suggests that dendrites interfered with the formation of a dominant shear front. The MGM-62V_f^C sample instead exhibited a convergence of the high strain region toward the center of the indenter just beneath the contact surface, thereby aligning with the maximum shear stress criterion. This crossover in the governing yield criterion demonstrates that at a crystalline phase fraction of approximately 60%, MGMCs exhibit a shift from a brittle deformation mode with plastic strain accumulation limited by shear localization to a more ductile response due to enhanced dislocation plasticity. From Fig. 1c, an increase in the crystalline phase fraction is accompanied by the formation of larger dendrites and interdendritic spacings. The homogeneous flow transition can thus be attributed to enhanced strain accommodation by the larger dendrites limiting shear localization in the amorphous matrix.

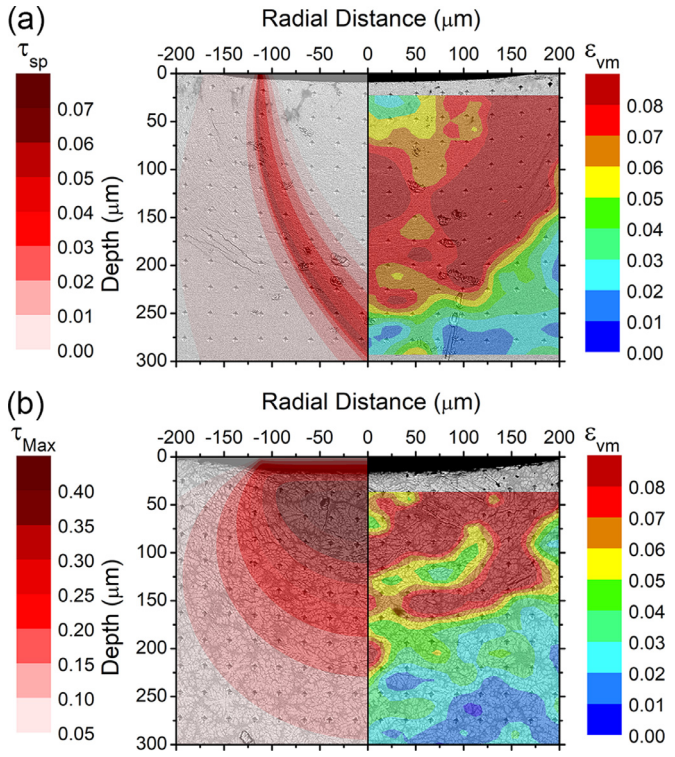

Fig. 4. Backscatter electron micrographs of the indented cross sections for (a) MGM-48V_f^C with the shear plane stresses plotted on the left and the experimental strain distribution on the right and (b) MGM-62V_f^C with the maximum shear stress criterion plotted on the left and strain distribution on the right. The high strain region near the edge of contact aligned with the maxiumum τ_{sp} path in (a) while the entire distribution shifted toward τ_{max} in (b).

In summary, a bonded-interface indentation technique was employed to map two-dimensional strain fields within the plastic zone from spherical surface indentation of MGMCs with varying microstructural length scales. With increasing crystallinity, radial and semi-spherical shear banding transitioned to more homogeneous deformation traces on the cross sections, indicative of a crossover in the dominant deformation mode of the composites. A comparison of yield criterion and experimental strain field maps for each composite revealed a shift in the governing yield criterion from the shear plane to maximum shear stress criterion at a crystalline fraction of approximately 60%, which aligned with the shift in the underlying deformation behavior. Collectively, our findings demonstrate the microstructural dependence of the incipient to homogeneous flow transition in MGMCs by mapping the crossover in the governing yield criterion and in turn, the dominant deformation mode of the composite.

Declaration of Competing Interest

The authors declare that they have no known competing financial interests or personal relationships that could have appeared to influence the work reported in this paper.

Acknowledgments

Support for this work was provided through the National Science Foundation under Award CMMI-1401662 with additional support from Award CMMI-1554411. The authors gratefully acknowledge students Nicholas Olynik and David Wang for their assistance in preparing the bonded-interface indentation samples. This research leveraged electron microscopy resources in the Center for Functional Nanomaterials, which is a US DOE Office of Science Facility at Brookhaven National Laboratory under Contract No. DE-SC0012704. D.C. Hofmann acknowledges support from NASA's Exploration Systems Mission Directorate under Contract no. NNH10ZTT001N. Part of this work was done at the Jet Propulsion Laboratory, California Institute of Technology, under contract with the National Aeronautics and Aerospace Administration.

References

[1] M.M. Trexler, N.N. Thadhani, Prog. Mater Sci. 55 (8) (2010) 759–839.
[2] T.C. Hufnagel, C.A. Schuh, M.L. Falk, Acta Mater. 109 (2016) 375–393.
[3] C.A. Schuh, T.C. Hufnagel, U. Ramamurty, Acta Mater. 55 (12) (2007) 4067–4109.
[4] J. Eckert, J. Das, S. Pauly, C. Duhamel, J. Mater Res. 22 (2) (2007) 285–301.
[5] D.C. Hofmann, J.Y. Suh, A. Wiest, G. Duan, M.L. Lind, M.D. Demetriou, W.L. Johnson, Nature 451 (7182) (2008) 1085–10U3.
[6] H. Choi-Yim, W.L. Johnson, Appl Phys. Lett. 71 (26) (1997) 3808–3810.
[7] J. Qiao, H. Jia, P.K. Liaw, Mater. Sci. Eng. R Rep. 100 (2016) 1–69.
[8] J.W. Qiao, A.C. Sun, E.W. Huang, Y. Zhang, P.K. Liaw, C.P. Chuang, Acta Mater 59 (10) (2011) 4126–4137.
[9] Y.S. Oh, C.P. Kim, S. Lee, N.J. Kim, Acta Mater. 59 (19) (2011) 7277–7286.
[10] B. Cheng, J.R. Trelewicz, Acta Mater. 117 (2016) 293–305.
[11] C. Fan, R.T. Ott, T.C. Hufnagel, Appl. Phys. Lett. 81 (6) (2002) 1020–1022.
[12] A.H. Hunter, V. Araullo-Peters, M. Gibbons, O.D. Restrepo, S.R. Niezgoda, W. Windl, K.M. Flores, D.C. Hofmann, E.A. Marquis, J. Microsc. 264 (3) (2016) 304–310.
[13] T.C. Hufnagel, C. Fan, R.T. Ott, J. Li, S. Brennan, Intermetallics 10 (11–12) (2002) 1163–1166.
[14] C.C. Hays, C.P. Kim, W.L. Johnson, Phys. Rev. Lett. 84 (13) (2000) 2901–2904.
[15] J.L. Cheng, G. Chen, F. Xu, Y.L. Du, Y.S. Li, C.T. Liu, Intermetallics 18 (12) (2010) 2425–2430.
[16] M.E. Launey, D.C. Hofmann, J.Y. Suh, H. Kozachkov, W.L. Johnson, R.O. Ritchie, Appl. Phys. Lett. 94 (24) (2009) 3.
[17] F. Abdeljawad, M. Fontus, M. Haataja, Appl. Phys. Lett. 98 (3) (2011).
[18] P.S. Singh, R.L. Narayan, I. Sen, D.C. Hofmann, U. Ramamurty, Mater. Sci. Eng. A-Struct. Mater. Prop. Microstruct. Process. 534 (2012) 476–484.
[19] R.L. Narayan, L. Tian, D.L. Zhang, M. Dao, Z.W. Shan, K.J. Hsia, Acta Mater 154 (2018) 172–181.
[20] H. Guo, P.F. Yan, Y.B. Wang, J. Tan, Z.F. Zhang, M.L. Sui, E. Ma, Nat Mater. 6 (10) (2007) 735–739.
[21] C.A. Schuh, T.G. Nieh, Acta Mater. 51 (1) (2003) 87–99.
[22] W.H. Jiang, M. Atzmon, J. Mater. Res. 18 (4) (2003) 755–757.
[23] B. Moser, J. Kuebler, H. Meinhard, W. Muster, J. Michler, Adv. Eng. Mater. 7 (5) (2005) 388–392.
[24] R. Limbach, K. Kosiba, S. Pauly, U. Kuhn, L. Wondraczek, J. Non-Cryst. Solids 459 (2017) 130–141.
[25] M.B. Harris, L.S. Watts, E.R. Homer, Acta Mater. 111 (2016) 273–282.
[26] C.A. Schuh, A.C. Lund, T.G. Nieh, Acta Mater. 52 (20) (2004) 5879–5891.
[27] J.M. Gentile, D.D. Stauffer, D.C. Hofmann, J.R. Trelewicz, Materialia 9 (2020) 100598.
[28] J.A. Kolodziejska, H. Kozachkov, K. Kranjc, A. Hunter, E. Marquis, W.L. Johnson, K.M. Flores, D.C. Hofmann, Sci. Rep. 6 (2016) 8.
[29] L. Zhang, R.L. Narayan, H.M. Fu, U. Ramamurty, W.R. Li, Y.D. Li, H.F. Zhang, Acta Mater 168 (2019) 24–36.
[30] H. Bei, Z.P. Lu, E.P. George, Phys. Rev. Lett. 93 (12) (2004) 4.
[31] K.W. Chen, J.F. Lin, Int. J. Plast. 26 (11) (2010) 1645–1658.
[32] Y.F. Gao, L. Wang, H. Bei, T.G. Nieh, Acta Mater. 59 (10) (2011) 4159–4167.
[33] S. Jana, R. Bhowmick, Y. Kawamura, K. Chattopadhyay, U. Ramamurty, Intermetallics 12 (10–11) (2004) 1097–1102.
[34] S. Jana, U. Ramamurty, K. Chattopadhyay, Y. Kawamura, Mater. Sci. Eng. A-Struct. Mater. Propert. Microstruct. Process. 375 (2004) 1191–1195.
[35] M.N.M. Patnaik, R. Narasimhan, U. Ramamurty, Acta Mater. 52 (11) (2004) 3335–3345.
[36] U. Ramamurty, S. Jana, Y. Kawamura, K. Chattopadhyay, Acta Mater. 53 (3) (2005) 705–717.
[37] B.G. Yoo, J.I. Jang, J. Phys. D Appl. Phys. 41 (7) (2008) 7.
[38] H.W. Zhang, X.N. Jing, G. Subhash, L.J. Kecskes, R.J. Dowding, Acta Mater 53 (14) (2005) 3849–3859.
[39] C.E. Packard, C.A. Schuh, Acta Mater. 55 (16) (2007) 5348–5358.
[40] D. Kammer, P.W. Voorhees, Acta Mater. 54 (6) (2006) 1549–1558.
[41] M.L. Lee, Y. Li, C.A. Schuh, Acta Mater. 52 (14) (2004) 4121–4131.
[42] H. Sun, K.M. Flores, Metall. Mat Trans. A 41 (7) (2010) 1752–1757.
[43] R.L. Narayan, K. Boopathy, I. Sen, D.C. Hofmann, U. Ramamurty, Scr. Mater 63 (7) (2010) 768–771.
[44] L. Prchlik, J. Pisacka, S. Sampath, Mater. Sci. Eng. A-Struct. Mater. Prop. Microstruct. Process. 360 (1–2) (2003) 264–274.
[45] C. Su, L. Anand, Acta Mater 54 (1) (2006) 179–189.
[46] F. Shimizu, S. Ogata, J. Li, Mater. Trans. 48 (11) (2007) 2923–2927.
[47] R.L. Narayan, P.S. Singh, D.C. Hofmann, N. Hutchinson, K.M. Flores, U. Ramamurty, Acta Mater. 60 (13) (2012) 5089–5100.